

## Evidence for intrinsic defects and nanopores as hotspots in 2D PdSe<sub>2</sub> dendrites for plasmon-free SERS substrate with a high enhancement factor

Tadasha Jena, Md Tarik Hossain, Upasana Nath, Manabendra Sarma, Hiroshi Sugimoto, Minoru Fujii, P. K. Giri

### Angaben zur Veröffentlichung / Publication details:

Jena, Tadasha, Md Tarik Hossain, Upasana Nath, Manabendra Sarma, Hiroshi Sugimoto, Minoru Fujii, and P. K. Giri. 2023. "Evidence for intrinsic defects and nanopores as hotspots in 2D PdSe<sub>2</sub> dendrites for plasmon-free SERS substrate with a high enhancement factor." *npj 2D Materials and Applications* 7 (1): 8.  
<https://doi.org/10.1038/s41699-023-00367-3>.

## ARTICLE OPEN



# Evidence for intrinsic defects and nanopores as hotspots in 2D PdSe<sub>2</sub> dendrites for plasmon-free SERS substrate with a high enhancement factor

Tadasha Jena<sup>1</sup>, Md Tarik Hossain<sup>2</sup>, Upasana Nath<sup>3</sup>, Manabendra Sarma<sup>3</sup>, Hiroshi Sugimoto<sup>4</sup>, Minoru Fujii<sup>4</sup> and P. K. Giri<sup>1,2</sup>✉

Surface-enhanced Raman spectroscopy (SERS), a very powerful tool for the identification of molecular species, has relied mostly on noble metal-based substrates to obtain a high enhancement factor. In this work, we demonstrate that self-driven intrinsic defects in 2D palladium di-selenide (PdSe<sub>2</sub>) dendrites grown at low temperature (280 °C) act as hotspots for high SERS enhancement. We grow 2D dendritic PdSe<sub>2</sub> with ample intrinsic defects to exploit it for SERS application. X-ray electron spectroscopy (XPS) analysis reveals 9.3% outer layer and 4.7% interior Se vacancies. A detailed examination of atomic-scale defects revealed Se vacancy (V<sub>Se</sub>) coupled with Se–Pd–Se vacancy (V<sub>Se-Pd-Se</sub>) in monolayer PdSe<sub>2</sub>, and an array of line defects (Se vacancies) and nanopores in bilayer PdSe<sub>2</sub> dendrites. Interestingly, our studies reveal that Se vacancy-rich PdSe<sub>2</sub> gives rise to line defects that act like hotspots for SERS enhancement. Remarkably, the vacancy-rich dendritic PdSe<sub>2</sub> shows a SERS enhancement factor >10<sup>5</sup> and can detect RhB at a concentration down to 10<sup>−8</sup> M. We speculate that the topological line defects and the edge construction in PdSe<sub>2</sub> dendrites act as metallic wire or edge, which is partly responsible for the high enhancement in the SERS signal. The high SERS sensitivity is explained on the basis of multiple charge transfer processes combined with the predicted metal-like behavior of the defected 2D PdSe<sub>2</sub>. Our conclusions are fully supported by the density functional theory calculation of the electronic density of states of the defective bilayer (2L) PdSe<sub>2</sub>, which remarkably exhibits metallic character. Being a defect-enabled SERS substrate, dendritic 2D PdSe<sub>2</sub> fills the gap between conventional plasmonic SERS substrate and plasmon-free SERS substrate.

npj 2D Materials and Applications (2023)7:8; <https://doi.org/10.1038/s41699-023-00367-3>

## INTRODUCTION

Recently, a new family of two-dimensional (2D) materials, namely noble transition metal di-chalcogenides (NTMDs) with atomic thickness, has received significant attention due to their unique properties, including thickness-dependent tunable-bandgaps that has potential for various optoelectronic applications<sup>1–6</sup>. PdSe<sub>2</sub> is one of the promising NTMDs due to its low symmetry lattice structure with highly tunable bandgap from 0 eV (bulk) to 1.43 eV (monolayer), high carrier mobility, high air stability with monolayer thickness ~0.5 nm<sup>7–9</sup>. PdSe<sub>2</sub> shows many distinctive properties, such as in-plane anisotropic properties similar to black phosphorus (BP)<sup>10</sup>. BP has been reported as a very promising material in nanotechnology<sup>11</sup>. However, poor stability in ambient conditions limits its application in various fields<sup>12</sup>. We anticipate that 2D PdSe<sub>2</sub> may replace the BP in many fields due to its in-plane anisotropy with high stability in ambient conditions.

For years on end, it was believed that defects would be structurally unstable in 2D crystals according to the Mermin–Wagner theorem<sup>13</sup>. Defect field traced a new trajectory when graphene layer was exfoliated and isolated in 2004<sup>14</sup>. Structural defects, including edges and point defects, have a significant influence on mechanical, thermal, optical, electrical properties in graphene and transition metal di-chalcogenides (TMDs). The physiochemical properties of monolayer and few-layer graphene are dependent on the defect type, defect environment, and arrangements<sup>15</sup>. Edges have been shown to weaken the mechanical strength and degrade the

electronic performance of graphene<sup>16</sup>. It is reported that PdSe<sub>2</sub> exhibits strong interlayer interactions, which are associated with defects<sup>17,18</sup>. Recently, theories predicted that PdSe<sub>2</sub> with Pd, as well as Se vacancies, are stable and Se vacancies are more energetically favorable than Pd vacancies<sup>19</sup>. However, the experimental evidence for the same has rarely been reported. In case of dendritic PdSe<sub>2</sub>, the presence of dendritic edges gives rise to different Pd and Se terminations with different zigzag and armchair edges. However, defects in PdSe<sub>2</sub> have rarely been explored compared to that in graphene and other TMDs<sup>8,20–23</sup>.

It is well known that defects and edges are beneficial for several applications; for example, defects are essential in creating bonding and trapping sites for atoms and molecules, which can be used for sensing applications<sup>24</sup>. In recent years, it has been reported that a non-SERS substrate can show SERS activity only by introducing defects<sup>25–27</sup>. This motivates us to exploit the defects in 2D PdSe<sub>2</sub> for possible application in SERS. Conventionally, high SERS activity mainly appears in hotspots of plasmonic noble-metal materials (mostly Au and Ag)<sup>28–34</sup>. However, there are many drawbacks of plasmonic-based SERS such as they require a well-designed hotspot, high cost, poor biocompatibility, low stability, which limits its applications in routinely used commercial products<sup>35</sup>. In comparison to traditional plasmonic-metal-based SERS, plasmon-free SERS substrates have attracted tremendous attention due to their excellent stability, low price, recyclability, superior biocompatibility, and many promising applications in the field of biomedical diagnosis<sup>36</sup>, metal ions

<sup>1</sup>Centre for Nanotechnology, Indian Institute of Technology Guwahati, Guwahati, Assam 781039, India. <sup>2</sup>Department of Physics, Indian Institute of Technology Guwahati, Guwahati, Assam 781039, India. <sup>3</sup>Department of Chemistry, Indian Institute of Technology Guwahati, Guwahati, Assam 781039, India. <sup>4</sup>Department of Electrical and Electronics Engineering, Kobe University, Rokkodai, Nada, Kobe 657-8501, Japan. ✉email: giri@iitg.ac.in

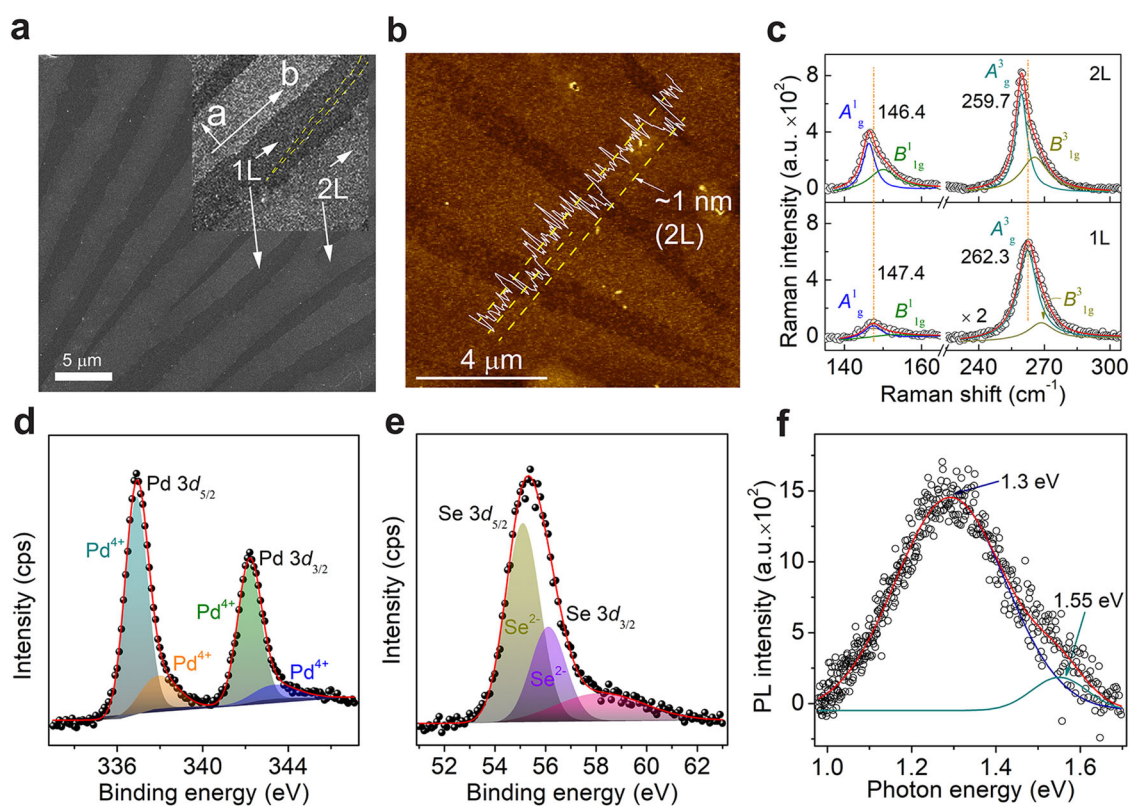


**Fig. 1 Morphology, composition and optical properties of dendritic 2D PdSe<sub>2</sub>.** **a** FESEM image of 1L and 2L PdSe<sub>2</sub>. The inset depicts the magnified view with dendrite propagation direction (along *a* axis and *b* axis). **b** AFM image with height profile of 2L (~1 nm), 1L (~0.5 nm) PdSe<sub>2</sub>, respectively. **c** Stacked Raman spectra with Lorentzian fit for 1L and 2L PdSe<sub>2</sub>, where symbols represent raw data and solid lines show fitted spectra. **d**, **e** XPS spectra of PdSe<sub>2</sub> dendrites for (d) Pd 3d and (e) Se 3d, with Shirley baseline fitted spectra. **f** NIR photoluminescence spectrum of PdSe<sub>2</sub> dendrites with Gaussian fitting.

and organic pollutant sensing<sup>37</sup>, monitoring in chemical reactions. At present, there exists a big gap between plasmonic SERS substrate and plasmon-free SERS substrate, as plasmonic SERS substrate often shows higher enhancement factors. Though SERS has been a very active area of research for decades, it remains challenging to reproduce plasmon-free SERS substrates with a high enhancement factor (EF)<sup>38</sup>. To our knowledge, no report contributed to the high SERS activity of 2D PdSe<sub>2</sub> dendrites enriched with intrinsic defects. Like SERS, in the field of nanopore sensing techniques, there is intense research to achieve nanopores in 2D material (graphene<sup>39</sup>, TMDs<sup>40</sup>, boron nitride<sup>29,41</sup>, black phosphorus<sup>42</sup>, etc.) instead of solid-state nanopores and biological nanopores due to their superior characteristics<sup>32,43</sup>. To our knowledge, there is no experimental report on the properties and applications of intrinsic defects and nanopores in 2D PdSe<sub>2</sub>. Till date, there is no report on the line defects in PdSe<sub>2</sub> and its exploitation in SERS sensing.

Herein, we report a two-step salt-assisted low-temperature (280 °C) CVD synthesized bilayer (2L) dendritic PdSe<sub>2</sub> and monolayer (1L) inter-dendritic region. In 2D PdSe<sub>2</sub>, two Se atoms in the top layer and two Se atoms in the bottom layer are joined by a tilted structure with one Pd in-between. Se atoms cover the outer surface by forming a protecting layer to PdSe<sub>2</sub>. We addressed high vacancies of upper Se atoms, as we know surface Se atoms can escape more easily. From the TEM and AFM image analysis, we report a systematic study on various defects, edge geometry, and nanopore in dendritic PdSe<sub>2</sub>. Near-infrared (NIR) PL studies revealed a decrease in bandgap in monolayer and bilayer dendritic PdSe<sub>2</sub>, which further supports the presence of Se vacancies. In addition, an additional peak in the XPS spectrum confirms the presence of defects in PdSe<sub>2</sub>. It is shown that defects,

nanopores, and edge geometry in dendritic PdSe<sub>2</sub> act as trapping/binding sites for foreign atoms/molecules. These active sites and vacancies play a crucial role in the enhanced Raman signal of Rhodamine B<sup>44</sup>. SERS signal-associated photoluminescence of RhB/PdSe<sub>2</sub> hybrid system confirms that the Se vacancy sites in defective dendritic PdSe<sub>2</sub> act as hotspots for SERS of RhB molecule. The density functional theory (DFT) calculations show that the inclusion of the Se-defect into the 2D PdSe<sub>2</sub> system alters its electronic behavior from semiconductor to metallic. Our results show that the topological line defect of Se<sub>TLU</sub> (top layer upper Se) in PdSe<sub>2</sub> in the presence of excess Pd behaves as metallic edges, which is responsible for the high SERS enhancement. Finally, we discuss the charge transfer mechanism in PdSe<sub>2</sub>/RhB based on the energy band diagram. This study addresses a unique 2D semiconducting nanostructure for SERS application, and it may fill the gap between conventional plasmonic SERS substrate and nonconventional plasmon-free SERS substrate, which was enabled by defect engineering in 2D NTMDs.

## RESULTS AND DISCUSSION

### Structure and morphology of dendritic PdSe<sub>2</sub>

The control of layer number in dendritic growth is crucial in 2D material synthesis. Controlled growth of 2L and 1L is obtained via our previously reported CVD technique with minor modification (refer to experimental methods for detailed information)<sup>45</sup>. Figure 1a illustrates the FESEM micrograph of the 2L PdSe<sub>2</sub> dendrites grown on the freshly cleaved mica substrate, which is enlarged (Fig. 1a, inset) for better visualization. The average width of 2–4 μm was mostly grown over the mica substrate. An optical microscopy image (Supplementary Fig. 1) shows the dendritic

pattern growth of 2D PdSe<sub>2</sub>, where the dendritic initiation zone has been shown. The PdSe<sub>2</sub> dendrites begin from the dendritic zone and move along the b direction. Dendritic PdSe<sub>2</sub> extends up to few tens of micrometers mostly along b direction, as confirmed in a later section. There exist an inter-dendritic region in-between 2L edges of bilayer PdSe<sub>2</sub>, which is barely visible from the magnified FESEM micrograph (inset Fig. 1a, yellow marked in the inset of FESEM micrograph). Later, 1L PdSe<sub>2</sub> islands in the inter-dendritic region are confirmed from Raman and TEM analyses. Atomic force microscopy (AFM) was employed to evaluate the detailed edge morphology with the thickness of the PdSe<sub>2</sub> layer. Raman mapping (Supplementary Fig. 2) also validates spatial uniformity over the 2L dendrites, and in-between 2L, there exist 1L PdSe<sub>2</sub> dendritic islands. Figure 1b shows the AFM image of PdSe<sub>2</sub> dendrites. AFM height profile analysis reveals a thickness of ~1 nm in the higher contrast region, whereas for regions in between two dendrites, it is ~0.5 nm. The consistency of contrast or height over the large area concludes the uniform growth of dendrites. Interestingly, the thickness of 1 nm corresponds to bilayer (2L) PdSe<sub>2</sub>, and ~0.5 nm corresponds to monolayer<sup>46</sup>. From the AFM image, we observe a highly rough surface of the PdSe<sub>2</sub> layer (estimated RMS roughness is ~0.5 nm), indicating its vacancy-contained mono and bilayer dendrite. A large number of nanopores are present in the dendritic PdSe<sub>2</sub> (discussed in a later section), which make the dendritic PdSe<sub>2</sub> surface porous and rough. Further, Raman spectra were acquired to understand the details of the crystallinity of 1L and 2L PdSe<sub>2</sub> (Supplementary Fig. 3). Figure 1c shows the stacked Raman spectra of 1L and 2L PdSe<sub>2</sub> with Lorentzian line-shape fitting. The fitting parameters are presented in Supplementary Table 1. The characteristics Raman modes  $A_1^1$ ,  $A_1^2$ ,  $A_1^3$ ,  $B_{1g}^1$ ,  $A_2^2$ ,  $B_{1g}^2$ ,  $A_3^3$ ,  $B_{1g}^3$  were observed in the 2L PdSe<sub>2</sub> dendrites (Supplementary Fig. 3). As the excitation source is unpolarized, we deconvoluted the highly intense peak  $A_1^3 - B_{1g}^3$  and  $A_3^3 - B_{1g}^3$  to understand the individual contribution of  $A_1^3$ ,  $B_{1g}^3$ ,  $A_3^3$ ,  $B_{1g}^3$  modes, respectively, similar to our earlier report<sup>45</sup>.  $A_1^3$  peak position ( $146.6\text{ cm}^{-1}$ ) in 2L PdSe<sub>2</sub> is redshifted ( $0.8\text{ cm}^{-1}$ ) compared to 1L  $A_1^3$  peak position ( $147.4\text{ cm}^{-1}$ ). It is obvious that a change in layer number leads to a change in phonon propagation behavior in the PdSe<sub>2</sub>. As the layer thickness shrinks, the scattered photon carries higher energy due to the relaxation in the Van der Waal stacked layers in PdSe<sub>2</sub>. In addition,  $A_3^3$  mode peak positions are  $259.7\text{ cm}^{-1}$  for 2L and  $262.3\text{ cm}^{-1}$  for 1L. The downward peak shift in  $A_3^3$  mode is  $2.6\text{ cm}^{-1}$  for the same reason. FWHM of peak  $A_1^3$  and  $A_3^3$  modes are  $5.6\text{ cm}^{-1}$  and  $10.7\text{ cm}^{-1}$  in 1L and  $4.0$  and  $6.5\text{ cm}^{-1}$  in 2L, respectively. The increase in FWHM for 1L compared to 2L may be attributed to the cumulative effects of higher surface defects with the decrease in layer number. Surface defects are more in 1L than 2L, as confirmed from EDX analysis (Supplementary Fig. 4a–f) of atomic percentage, where we can see the magenta rectangle enclosed the 2L edge along with 1L (Supplementary Fig. 4e). Se atomic percentage is very low at the edge of the 2L (Supplementary Fig. 4f) than in the middle 2L region (Supplementary Fig. 4d). To understand the surface property, we further carried out XPS measurements. The XPS survey spectrum (Supplementary Fig. 5) highlights the presence of Pd, Se, C, O. Figure 1d, e shows the Pd 3d and Se 3d high-resolution spectra with Gaussian peak fitting (Shirley baseline). The peak positions at 336.9 eV and 342.2 eV exhibit binding energy of the Pd<sup>4+</sup> state, which originates due to Pd 3d<sub>5/2</sub> and Pd 3d<sub>3/2</sub> core label emission, respectively. The value corresponding to Pd 3d<sub>5/2</sub> is comparatively less than the reported value<sup>47</sup>. This discrepancy in the binding energy might be attributed to the following reasons. The low-temperature grown PdSe<sub>2</sub> dendrites contain several types of intrinsic defects. A careful observation of Supplementary Fig. 1 reveals that there is an initiation zone where the PdSe<sub>2</sub> dendrites originate. At first, the bulk PdSe<sub>2</sub> acts as a Pd

source region. From this initiation zone, 2L PdSe<sub>2</sub> dendrites start growing and end up with 1L PdSe<sub>2</sub>. The structure of the PdSe<sub>2</sub> is very different from other TMDs, where the Se–Se tilted layer crosses the Pd layer (Supplementary Fig. 6). This type of structure is highly sensitive towards intrinsic defects due to the break in the symmetry of Se–Se bond<sup>21</sup>. As the layer number of PdSe<sub>2</sub> decreases, a significant number of Se atoms are exposed and may detach from the surface, which gives rise to abundant Se vacancies in 2L and 1L dendrites. Further, the electronegativity of Se is lower than oxygen; as the vacancies increase, Se requires lower binding energy to break the Pd–Se bond. As the sample is exposed to atmospheric conditions, it forms a Pd–O bond by atmospheric oxygen in place of Se vacancies. Due to the above, two additional peaks at 337.8 eV and 343.4 eV are observed and are attributed to the formation of Pd–O bond<sup>48</sup>. It clearly indicates that there exists a high density of Se vacancies in PdSe<sub>2</sub> dendrites. The binding energy peaks of Se 3d spectra consist of Se 3d<sub>5/2</sub> (55.1 eV) and Se 3d<sub>3/2</sub> (56.1 eV). Areal analysis of XPS reveals 9.3% outer Se vacancies, 4.7% inner Se vacancies, and 4.7% Pd vacancies in dendritic PdSe<sub>2</sub>. In the later section, a thorough discussion on vacancies and edge construction on dendritic PdSe<sub>2</sub> is presented and we show that, Se<sub>TLU</sub> (upper layer top Se) vacancies are highest in dendritic PdSe<sub>2</sub>. Deconvoluted peaks show an additional peak at 58.2 eV due to Se–O bond formation<sup>47</sup>. Non-bonded Se atoms in one side and Se adatoms at the dendritic edge, and fewer Pd vacancies contributed to this peak. From the above analysis, we may conclude that an abundant number of Se vacancies and comparatively fewer Pd vacancies exist. Further, NIR photoluminescence (PL) measurement of as-grown PdSe<sub>2</sub> was carried out with 641 nm laser excitation. Figure 1f displays the PL spectrum with fitted two Gaussian peaks centered at 1.3 eV and 1.55 eV. As discussed earlier, there are many Se vacancies; as a result, the bandgap is reduced and it requires less photon energy to excite the electron. Depending on the concentration of vacancies, the bandgap decreases. For example, Kuklin et al. reported one vacancy per 4 unit cells of monolayer PdSe<sub>2</sub> characterized by an energy gap of 0.67 eV, whereas one vacancy per 16 unit cells corresponds to a bandgap of 1.03 eV<sup>2</sup>. As a result of BZ lifting and depending on the number of Se vacancies in monolayer and bilayer PdSe<sub>2</sub>, the bandgap decreases to 1.3 eV for monolayer. In addition, it was stated that the optical bandgap of non-defective 2L PdSe<sub>2</sub> is 1.89 eV and that of defective 2L PdSe<sub>2</sub> is 1.55 eV. Our experimental finding revealed a bandgap of 1.55 eV for defective 2L PdSe<sub>2</sub> dendrites, which is the same as the reported theoretical value of defective PdSe<sub>2</sub><sup>2</sup>. Unlike other TMDs (such as MoS<sub>2</sub>), 1L PdSe<sub>2</sub> shows comparatively higher FWHM (0.3 eV) in the PL spectrum, which may be due to the presence of defects and partly due to the distribution in the number of layers. Other possible reasons for the higher FWHM are: (1) the anisotropic lattice structure of PdSe<sub>2</sub>, and (2) ten valence electrons in each Pd, which is higher than conventional TMDs. The low-intensity peak at 1.55 eV may be arising from the 2L PdSe<sub>2</sub> and/or recombination of carriers at the defects in PdSe<sub>2</sub>.

### Defects and edge construction

Based on the signature of defects in PdSe<sub>2</sub> dendrites from XPS and PL, we undertook a detailed study of defects from electron microscopic analyses. Figure 2a illustrates the dark-field TEM image of three consecutive dendrites. The EDX mapping of Pd and Se is shown in Fig. 2b, c, respectively. The EDX mapping over a small area of brightfield TEM image is shown in Supplementary Figs. 7 and 8. A careful observation of the white-shaded region in the mapping reveals that Pd:Se proportion increases at the end of the dendrites, implying increasing Se vacancies at the end of the dendrite. Figure 2d shows the atomic percentage of Pd and Se from EDX, which further confirms the presence of Se vacancies. In order to find the percentage of Se vacancies in the 2L middle,

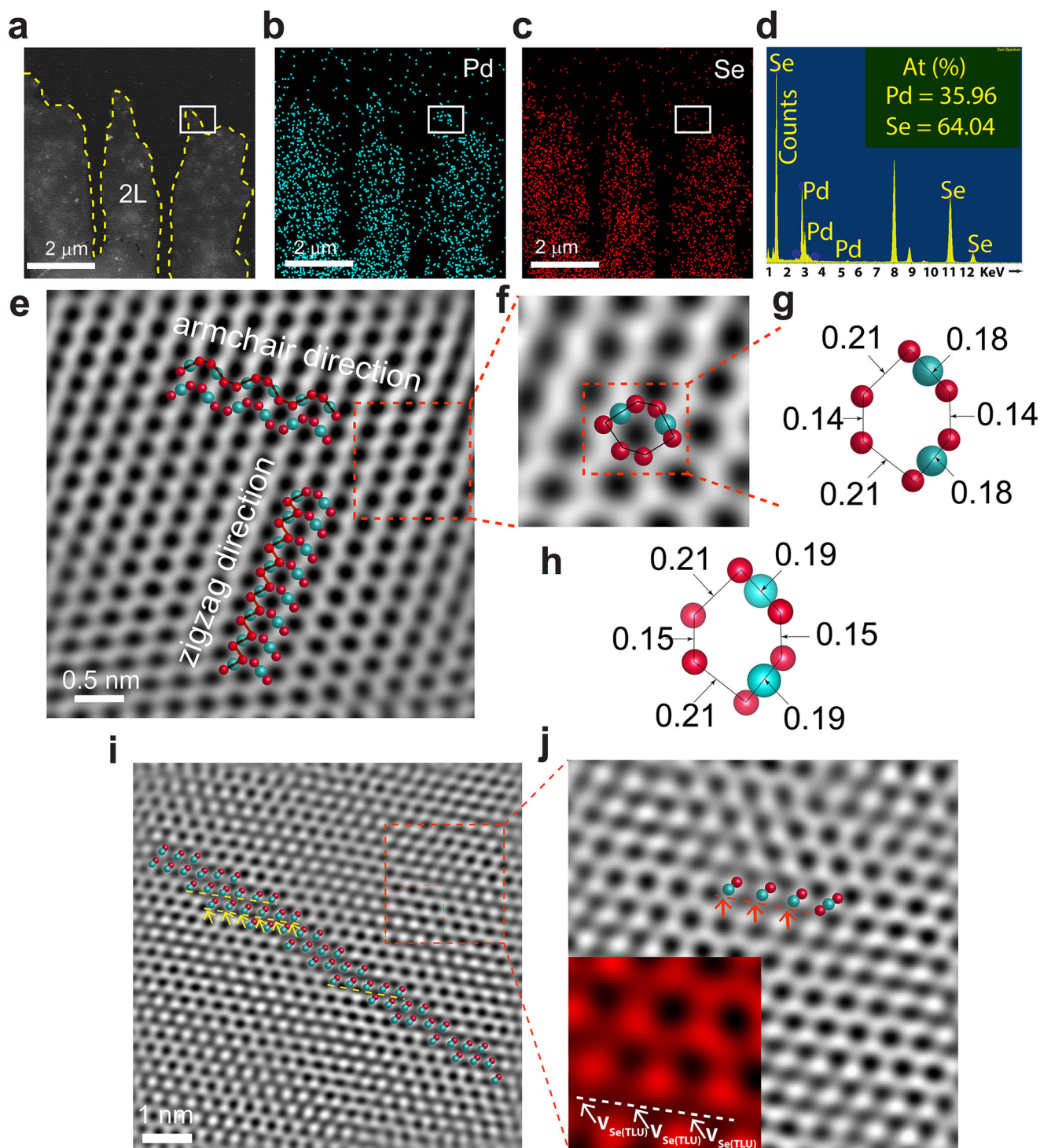


**Fig. 2** TEM imaging of line defects in dendritic PdSe<sub>2</sub>. **a** Dark-field TEM image of PdSe<sub>2</sub> dendrites, **b**, **c** the elemental distribution of Pd and Se, respectively; **d** the corresponding atomic percentage spectrum. **e** HRTEM image of defect-free 2L PdSe<sub>2</sub> including armchair and zigzag edges. **f** Magnified view of HRTEM image with the atomic arrangement. **g** Atomic model representation with interatomic distance of experimental data. **h** Theoretically obtained 2D interatomic distance in the atomic model. **i** HRTEM image of defective 2L PdSe<sub>2</sub> including series of line defects. **j** Magnified view of defective 2L PdSe<sub>2</sub> showing line defects; arrow indicates Se<sub>TLU</sub> vacancies, which disrupts the hexagonal structure.

2L edge, and 1L, EDX spectra were collected in different regions (Supplementary Fig. 4). In Supplementary Fig. 4a, c, and e, spectra were recorded over a small region in the middle of 2L dendrite, a slightly larger area in the 2L dendrite, and a comparatively large area consisting of the edge of 2L dendrites as well as monolayer PdSe<sub>2</sub>, respectively. From the atomic %, we believe that the vacant

Se atom in the monolayer and the edge sites of PdSe<sub>2</sub> are responsible for the highest Se vacancy in Supplementary Fig. 4e. In Supplementary Fig. 4a, the density of vacancy in a small area is relatively less than in Supplementary Fig. 4c. In Supplementary Fig. 4a, there are fewer Se vacancies, whereas Supplementary Fig. 4c contains much Se vacancies due to existence of nanopores, which

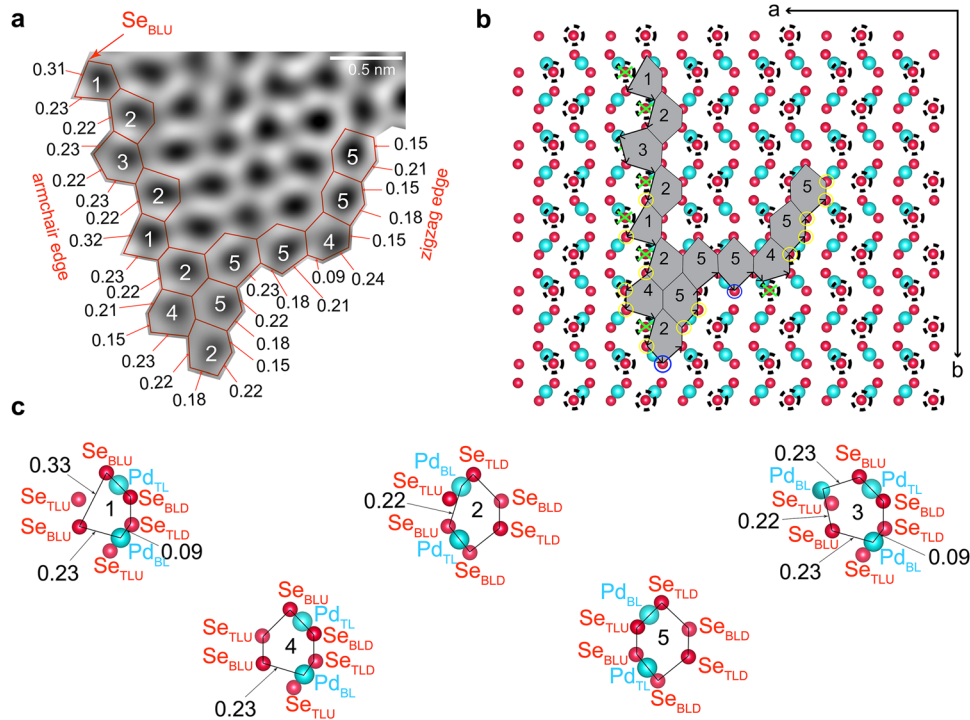


**Fig. 3** Edge construction of dendritic PdSe<sub>2</sub> edge. **a** High-resolution TEM image of 2L PdSe<sub>2</sub> dendrites with measured edges in nanometers. **b** Theoretical model showing edge geometry of 2L dendritic PdSe<sub>2</sub>, where black circles encircling the Se atoms denotes Se<sub>TLU</sub>, yellow circle encircling Se denotes one side non-bonded Se-Pd, blue circle encircling Se are Se<sub>BLU</sub> atoms, green cross mark denotes excluded Se<sub>TLU</sub> from the followed path. **c** Theoretically calculated interatomic distance (in nm), which matches well with the experimentally obtained interatomic distance from HRTEM.

are discussed later. The HRTEM image of 2L PdSe<sub>2</sub> dendrite is shown in Fig. 2e, where hexagonal PdSe<sub>2</sub> (h-PdSe<sub>2</sub>) is clearly visible. One h-PdSe<sub>2</sub> contains six Se atoms and two Pd atoms. For better understanding, we divided them into top layer up Se (Se<sub>TLU</sub>), top layer down Se (Se<sub>TLD</sub>), bottom layer up Se (Se<sub>BLU</sub>), bottom layer down Se (Se<sub>BLD</sub>), and top layer Pd (Pd<sub>TL</sub>), bottom layer Pd (Pd<sub>BL</sub>), as shown in Supplementary Fig. 6. From the HRTEM image, we can get a two-dimensional picture of the structure. An enlarged view of a selected area of Fig. 2e is shown in Fig. 2f. From intensity contrast and distance measurement in Fig. 2f, we obtained the arrangement of atoms with atomic distance as follows, Se<sub>BLU</sub>-Se<sub>TLU</sub> (tilted) = 0.21 nm, Se<sub>TLU</sub>-Se<sub>BLU</sub> (vertical) = 0.14 nm, Se<sub>TLU</sub>-Se<sub>TLD</sub> (tilted) = 0.18 nm, Se<sub>BLU</sub>-Se<sub>BLD</sub> (tilted) = 0.18 nm (shown in Fig. 2g), which are consistent with the theoretical calculated values (shown in Fig. 2h). Figure 2i illustrates a series of line defects with Se vacancies at the middle of 2L PdSe<sub>2</sub>. These Se vacancies are mainly Se<sub>TLU</sub> atoms, which are confirmed by HRTEM intensity analysis. To better visualize the Se<sub>TLU</sub> vacancies, a small area of Fig. 2i is shown in Fig. 2j. As revealed by the HRTEM image (Fig. 2e), dendrites with the simplest edge orientation are mainly two types, armchair, and zigzag. However, when we move to the edge part of the dendrite, we observe different armchair and zigzag edges. Like defects, edge geometry also plays an important role in the properties of nanomaterials. Hence, it is relevant to know PdSe<sub>2</sub> edge geometries and their chemical properties beyond standard zigzag and armchair ones. Based on calculations and measurements, we found that edge construction is different at the edge of the 2L dendrite (Fig. 3a). Dendrites possess mainly two types of edge structure, (1) armchair with pentagon and hexagon (one side pentagon, other side hexagon) and (2) zigzag with hexagons. We have analyzed the edge structure of a portion of the dendrite, shown in Fig. 3a, with the help of the atomic model shown in Fig. 3b. Figure 3a is the HRTEM image of the 2L dendritic edge. The corresponding brightfield high-resolution TEM image of 2L PdSe<sub>2</sub>

dendritic edge of Fig. 3a is shown in Supplementary Fig. 9. As the HRTEM image is two-dimensional, we have measured the two-dimensional distances of the edge in nanometers (shown in Fig. 3a). To know how the edge construction happens, we have first calculated each side of edge hexagons and pentagons (1 is a pentagon, and 2, 3, 4, 5 are hexagons) from the HRTEM analysis of Fig. 3a. These calculated sides from the HRTEM analysis are nearly the same as the theoretically calculated distances given in Fig. 3c, which are different from the normal defect-free hexagon sides (shown in Fig. 2g). Assuming the path initiation atom as Se<sub>BLU</sub>, we have followed the distance from one atom to another in the atomic model and traced the path. For example, starting with Se<sub>BLU</sub>, if Se<sub>BLU</sub> follows the next Se<sub>TLU</sub> then the distance will be 0.21 (from Fig. 2g). However, the distance of the next atom from Se<sub>BLU</sub> at the edge is 0.33 (in the HRTEM image Fig. 3a). If we exclude Se<sub>TLU</sub>, then Se<sub>BLU</sub> to the next Se<sub>BLU</sub> distance is 0.33 nm. Similarly, we have traced the entire edge construction of the dendritic PdSe<sub>2</sub>. Assuming the edge growth from pentagon 1 with Se<sub>BLU</sub>, it follows the path excluding mostly edge Se<sub>TLU</sub> atoms. The green cross marks are excluded Se<sub>TLU</sub> from the followed path of the edge construction. In pentagon 1, it follows the path excluding 2 Se<sub>TLU</sub>, and the distance between Se<sub>BLU</sub> to Se<sub>BLU</sub> in Fig. 3c is 0.33 nm, the distance between Se<sub>BLU</sub> to Pd<sub>BL</sub> (Se<sub>BLU</sub>-Pd<sub>BL</sub>) is 0.23 nm, and Pd<sub>BL</sub>-Se<sub>TLD</sub> = 0.09 nm. In hexagon 2, it follows the path excluding one Se<sub>TLU</sub>, where Pd<sub>BL</sub>-Se<sub>BLU</sub> = 0.22 nm. In hexagon 3, it follows the path excluding two Se<sub>TLU</sub>, where Se<sub>BLU</sub>-Pd<sub>BL</sub> (next hexagon Pd) = 0.23 nm, Pd<sub>BL</sub>-Se<sub>BLU</sub> = 0.22 nm. In hexagon 4, it follows the path excluding one Se<sub>TLU</sub>, where Se<sub>BLU</sub>-Pd<sub>BL</sub> = 0.23 nm. In hexagon 5, nothing is excluded. Starting from pentagon 1 Se<sub>BLU</sub> (encircled in blue), it follows a path as follows, Se<sub>BLU</sub> → Se<sub>BLU</sub> → Pd<sub>BL</sub> → Se<sub>BLU</sub> → Pd<sub>BL</sub> → Se<sub>BLU</sub> → Pd<sub>BL</sub> → Se<sub>BLU</sub> → Se<sub>BLU</sub> → Se<sub>BLU</sub> → Pd<sub>BL</sub> → Se<sub>BLU</sub> → Se<sub>TLU</sub> → Se<sub>BLU</sub> → Pd<sub>BL</sub> → Se<sub>BLU</sub> → Pd<sub>TL</sub> → Se<sub>BLD</sub> → Se<sub>TLD</sub> → Se<sub>BLD</sub> → Pd<sub>TL</sub> → Se<sub>BLU</sub> → Se<sub>TLU</sub> → Se<sub>BLU</sub> → Pd<sub>TL</sub> → Se<sub>BLD</sub> → Se<sub>TLD</sub> → Pd<sub>BL</sub> → Se<sub>BLU</sub> → Se<sub>TLU</sub> → Pd<sub>BL</sub> → Se<sub>TLD</sub> → Se<sub>BLD</sub> → Se<sub>TLD</sub> → Se<sub>BLD</sub>.

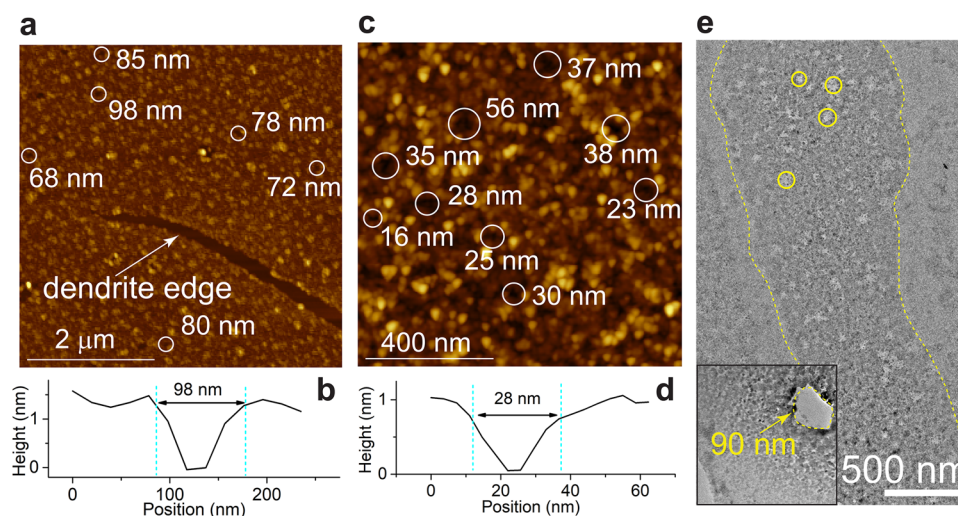


**Fig. 4** Nanopores in dendritic PdSe<sub>2</sub>. **a** Atomic force microscopy image showing the nanopores with pore diameters in the range 68–98 nm in 2L PdSe<sub>2</sub>. **b** Line profile showing the diameter of 98 nm for a nanopore. **c** White circles enclosed nanopores with an average diameter ranging from 16–56 nm in 2L PdSe<sub>2</sub>. **d** Line profile measures the diameter of 28 nm of a nanopore. **e** Brightfield low-resolution TEM image of 2L PdSe<sub>2</sub> with nanopores (yellow circled), and the inset reflects nanopores with an average diameter of 90 nm.

All the calculated atomic distances from the HRTEM image match well with the theoretically calculated values shown in Fig. 3c. In PdSe<sub>2</sub>, each Se is bonded with one Se and two Pd atoms (Se–Pd). But, at the edge of the dendrite, there exist many Se atoms where one Se–Pd bond is absent (Fig. 3b). The yellow circled Se atoms are bonded with one Pd atom at the edge, and one Pd–Se bond is absent. From the statistics, we concluded that 90% of edge Se atoms are bonded with only one Se–Pd bond at the edge of the dendrite. Active sites mainly exclude Se<sub>TLU</sub> atoms, which is due to the fact that Se<sub>TLU</sub> atoms can be removed more easily than other atoms. The most common defect is the single missing atom, called single vacancy (SV). In the case of PdSe<sub>2</sub> dendrite, we did not observe any SV from experimentally obtained TEM images. Most vacancies are associated with 2/3 V<sub>Se</sub> in the same row/column. Removal of more than two atoms leads to a more complex defect configuration. When the vacancy is created, the displaced atom may remain on the surface of the PdSe<sub>2</sub> layer as an adatom. Vacancies and adatoms are relatively mobile, but still unstable against recombination. From the end of the dendrite, we can notice that Se is at the propagating tip, which suggests Pd-edge is the initial nucleation edge which then is propagated by Se (Fig. 3b). However, there exist two Se adatoms at the tip of the edges encircled with blue line. The dendritic head consists of adatom, which might be the cause of ending the dendritic growth in that particular direction. Supplementary Fig. 10 illustrates the tilted side view of monolayer PdSe<sub>2</sub>. TEM imaging depends on the orientation of the material (crystal) with respect to the electron beam direction. From Supplementary Fig. 10, we can distinctly visualize the slightly tilted pattern of monolayer PdSe<sub>2</sub>. We confirmed it as a monolayer by analyzing the HRTEM image intensities. In fact, it is not easy to visualize the pentagonal shape because with the tilted view of PdSe<sub>2</sub>, we can see some rectangular patterns PdSe<sub>2</sub> from the tilted top (shown in Supplementary Fig. 10e). Supplementary Fig. 10c indicates a total of three Se with one Pd vacancy in monolayer PdSe<sub>2</sub>. TEM imaging enables us to identify a V<sub>Se</sub> (mono Se vacancy) along with V<sub>Se-Pd-Se</sub> (1 upper Se 1 Pd and 1 lower Se) atom vacancy from image intensity analysis (Supplementary Fig. 10d). Here, we notice that the vacancy exhibits closely a circular shape of about 1 nm in diameter. In monolayer PdSe<sub>2</sub>, we obtained two outer Se vacancies, one Pd vacancy along with one inner Se vacancy. Banhart et al. reported that vacancies with an even number of missing atoms are energetically favorable over an odd number of

missing atoms in graphene<sup>49</sup>. Similar to graphene, in PdSe<sub>2</sub>, mainly Pd vacancy occurs along with inner Se vacancies as an even number of vacancies are energetically favored, and more energy is required to break the Pd–Se bond. Our XPS analysis disclosed that there exist 9.3% outer Se vacancies, 4.7% Pd vacancies, 4.7% inner Se vacancies in dendritic PdSe<sub>2</sub>. XPS analysis supports our TEM image analyses, where outer Se vacancies are dominated, whereas Pd vacancy is always associated with inner Se vacancy. In bilayer PdSe<sub>2</sub>, we observe mainly Se<sub>TLU</sub> vacancies or sometimes Se<sub>BLU</sub> vacancies. Most Pd vacancies are not seen in Fig. 2i, j. We did not observe isolated Pd vacancy as Pd drags inner Se atoms. This is the key reason behind nanopore formation in 2L PdSe<sub>2</sub>. Making a nanopore in PdSe<sub>2</sub> without any post-growth treatment and without using the electron beam radiation technique is challenging<sup>50,51</sup>. We report a reliable, straightforward approach to synthesizing dendritic PdSe<sub>2</sub> with distributed nanopores. We consider these nanopores nearly circular, with diameters ranging from 10 to 90 nm (Fig. 4a, c, e). Figure 4a, c shows the AFM image of dendrites with distributed nanopores in a 1 nm thickness PdSe<sub>2</sub> dendrite. Figure 4b, d depicts height well for the estimation of nanopore diameters. Figure 4e shows the TEM image of a dendrite with many nanopores. The inset shows a magnified view of a ~90 nm diameter nanopore. We can differentiate between reported nanopores (where voids are formed by electron beam radiation) and our nanopores (without any treatment). Nanopores in PdSe<sub>2</sub> adopt an approximately pentagonal geometry with well-defined edges (shown in the inset of Fig. 4e). With the change in the ratio of PdCl<sub>2</sub> to NaCl during the growth, we observe different sizes of nanopores and defects (Supplementary Fig. 11). We exploit the vacancy-rich nanoporous 2D PdSe<sub>2</sub> dendrites for SERS applications, as discussed below.

#### Application of dendritic PdSe<sub>2</sub> in SERS sensing

Thanks to the fingerprint of Raman spectroscopy due to its remarkable sensitivity and chemical specificity. We have investigated the surface-enhanced Raman scattering (SERS) of RhB on PdSe<sub>2</sub> dendrites grown on a mica substrate. To investigate the individual contribution of 2L edge, 1L vacancy, and nanopore on SERS, we carried out position-dependent SERS measurements in three different regions. Figure 5a represents the broad range Raman spectrum of 10<sup>-5</sup> M RhB on the edge of 2L PdSe<sub>2</sub> dendrite. The presence of all the characteristic Raman modes of PdSe<sub>2</sub>, including SERS of RhB molecule, makes it very interesting to find

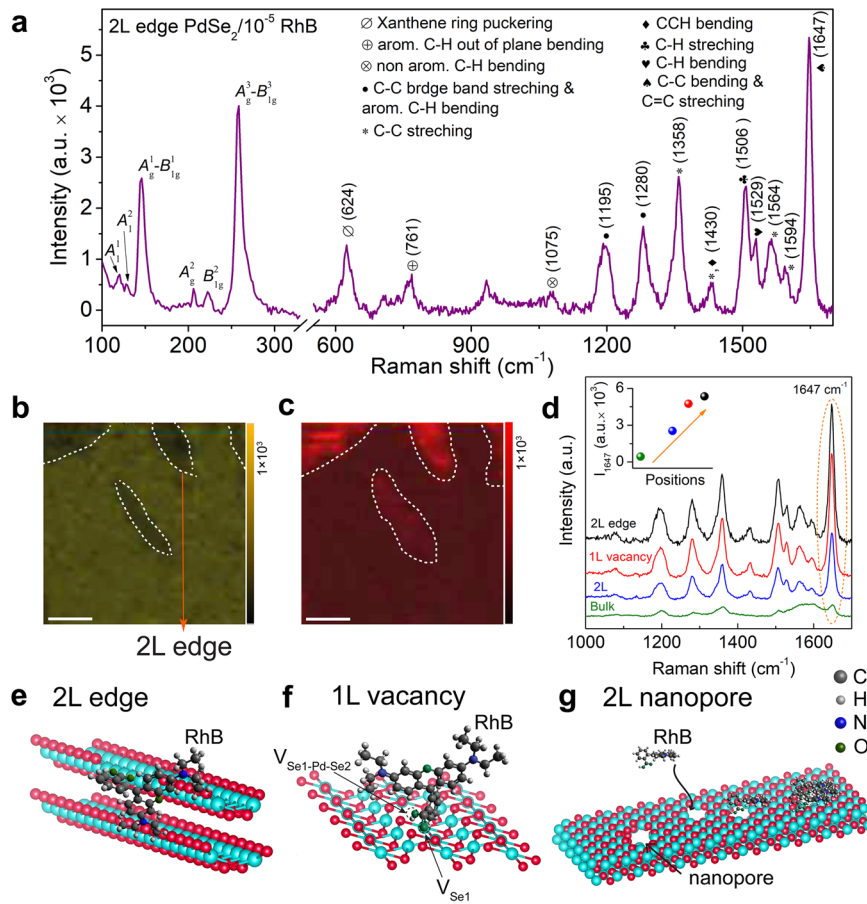
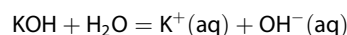


**Fig. 5 SERS enhancement at the dendritic PdSe<sub>2</sub>.** **a** Raman spectrum of 10<sup>-5</sup> M RhB on the intrinsic edge of 2L PdSe<sub>2</sub>. **b, c** The Raman intensity mapping of 258 cm<sup>-1</sup> peak of PdSe<sub>2</sub> and 1647 cm<sup>-1</sup> peak of rhodamine B, respectively. Scale bar is 2 μm. **d** Stacked Raman spectra of 10<sup>-5</sup> M RhB on different spots (2L edge, 1L vacancy, 2L surface, bulk). Inset shows the position-dependent Raman intensity ( $I_{1647}$ ). Proposed mechanism of adsorption of RhB molecules at three different sites: **e** 2L edge, **f** 1L vacancy and **g** 2L nanopores.

the origin of SERS sensing in novel PdSe<sub>2</sub> dendrites. Raman mapping was carried out on dendritic PdSe<sub>2</sub>/RhB for better visualization of defect-induced hotspots, which are believed to be responsible for the SERS enhancement, and it is added in Fig. 5b, c. Figure 5b shows the Raman intensity mapping of 258 cm<sup>-1</sup> peak of PdSe<sub>2</sub>, where uniform contrast is observed all over the dendritic PdSe<sub>2</sub>, but contrast changes at 2L edges. The signature of rhodamine B (1647 cm<sup>-1</sup>) was taken into consideration to obtain the Raman mapping of rhodamine B. Figure 5c shows the Raman mapping of 1647 cm<sup>-1</sup> peak of rhodamine B, where distinct brighter islands are found at the 2L edge of dendritic PdSe<sub>2</sub>. Interestingly, edge sites of PdSe<sub>2</sub> dendrites act as a kind of hotspot, and rhodamine B adsorption takes place at the Se vacant sites with Pd chains at the edge sites. Figure 5d shows the corresponding stacked Raman spectra of particular 2L edge, 1L vacancy, 2L middle portions of the dendrite, and bulk PdSe<sub>2</sub>. Inset shows the ascending order of peak intensities of characteristic Raman mode corresponding to C–C bending and C=C stretching (1647 cm<sup>-1</sup>). Figure 5d reveals a huge variation in intensities ( $I$ ) between bulk PdSe<sub>2</sub> and dendritic PdSe<sub>2</sub> (2L edge, 1L vacancy, 2L middle). Clearly,  $I$  (2L edge) >  $I$  (1L vacancy) >  $I$  (2L middle) >  $I$  (bulk). Among these, the 2L edges exhibit the highest intensity peak, which implies its highly sensitive nature toward SERS. It clearly indicates that active edges, defects, and nanopores play a vital role in SERS activity. Let us first consider the case of a 2L dendritic edge. 2L PdSe<sub>2</sub> edge is mostly terminated with one side bonded Se atoms as concluded from the TEM analysis (one Se–Pd bond is absent) (Fig. 3b). If an even number of atoms are removed

from the dendritic edge, then bonds can be healed to preserve the connectivity. If an odd number of atoms are removed, a bond exists that makes the structure most unstable and more chemically active. Koskinen et al. reported that an armchair edge with pentagons (Ac 56) is the most expensive edge with the highest edge energy in graphene<sup>52</sup>. Lu et al. reported that Se-ac (110) is the most stable edge in 2L PdSe<sub>2</sub><sup>10</sup>. Our PdSe<sub>2</sub> edge geometry mainly consists of Se-armchair (Se-ac), which suggests us believe that it is an exclusive as well as stable edge. Edge stress can be relieved by the addition of other atoms at the stable edges<sup>53</sup>. As discussed earlier, one Se–Pd bond is absent at the active sites, enhancing the dipole–dipole interaction between Se and C = N<sup>+</sup> (as N<sup>+</sup> ion in RhB acts as an electron deficiency site) of the RhB molecule. (Schematically shown in Fig. 5e–g). The positively charged C = N<sup>+</sup> group in the RhB molecule will be attracted by the negatively charged Se atoms at the active edge sites. As RhB is a zwitterionic molecule, further adsorption of the RhB molecule will happen in a head-to-tail manner. To further validate the above concept, we have done an EDX analysis at three different zones. Dendritic PdSe<sub>2</sub> is dipped into KOH solution overnight in the transfer process. In an aqueous solution, KOH dissociates to form K<sup>+</sup> ion.



Interestingly, K<sup>+</sup> adsorption happens in vacancy and edge sites of PdSe<sub>2</sub>, which is confirmed by EDX. EDX analysis showed that the dendritic PdSe<sub>2</sub> contains Pd, Se, K. These results further support

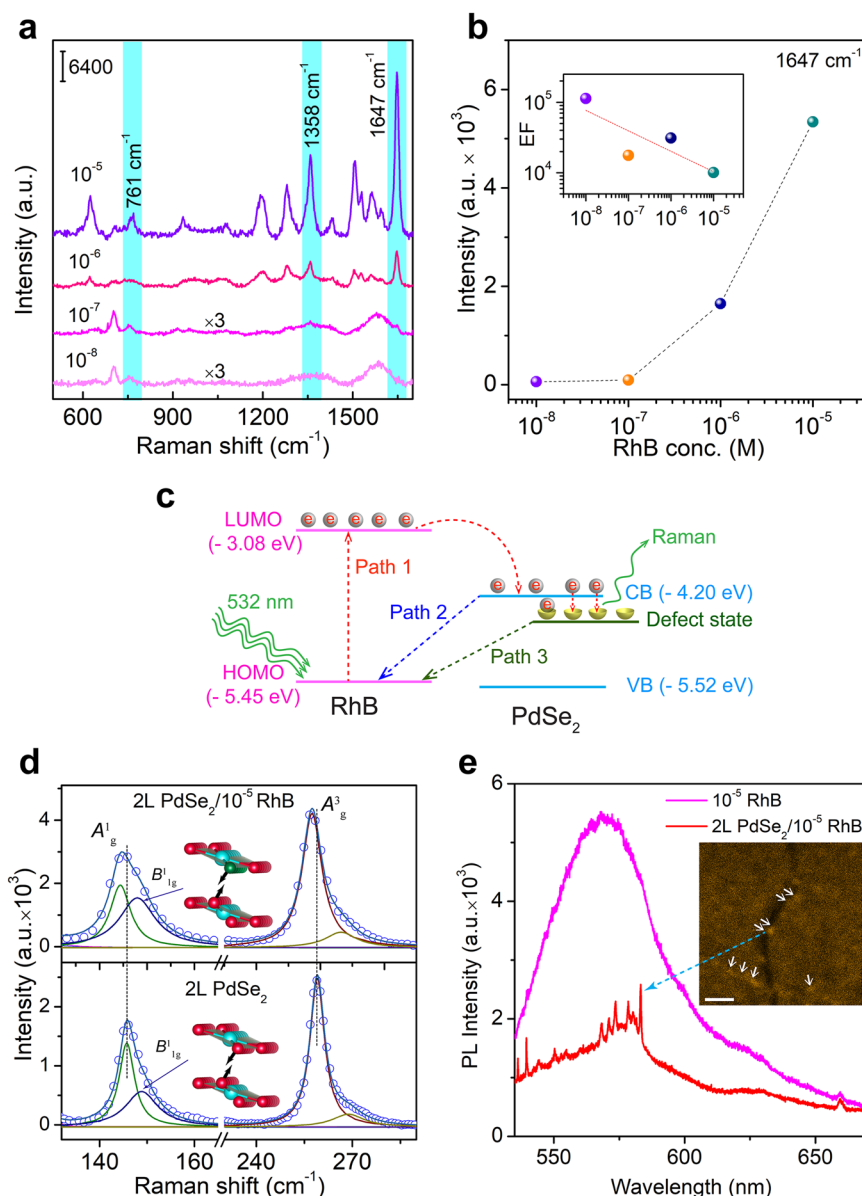


**Fig. 6 SERS enhancement factor and its mechanism.** **a** Raman spectra of  $10^{-5}$  M,  $10^{-6}$ ,  $10^{-7}$ ,  $10^{-8}$  M RhB on PdSe<sub>2</sub>, **b** the corresponding intensity semi-log plot for C–C bending and C = C stretching as a function of RhB concentration. The inset shows the log plot of calculated enhancement factor (EF). **c** Energy band diagram showing the charge transfer pathways in RhB/PdSe<sub>2</sub> hybrid system. **d** Stacked Raman spectra of 2L PdSe<sub>2</sub> and  $10^{-5}$  RhB drop-casted 2L PdSe<sub>2</sub>, where the inset atomic models show the  $B_{1g}^1$  vibrational mode. **e** Measured photoluminescence spectra of  $10^{-5}$  M RhB on mica substrate and SERS spectrum of 2L PdSe<sub>2</sub>/ $10^{-5}$  RhB. The inset shows the confocal microscopy image of RhB molecules on the defective sites (scale bar: 5  $\mu$ m).

the validity of the above possible route. EDX analysis at two different locations (2L middle, 2L edge) of the PdSe<sub>2</sub> dendrites are shown in Supplementary Fig. 8. K atomic percentage is highest at the edge of the dendrites, which indirectly confirms K<sup>+</sup> adsorption is more at the 2L edge and 1L. It is interesting to note that the sum of Se and K atomic percentages is exactly double the Pd atoms. This implies that Se vacancy at the active site act as a bonding site for K atoms. In the middle of a 2L dendrite, K adsorption happens with less atomic percentage (Supplementary Fig. 8). As K<sup>+</sup> and N<sup>+</sup> are positive ions, we can expect similar phenomena for the adsorption of N<sup>+</sup> ions. Thus, it indirectly indicates that the bonding of C = N<sup>+</sup> of RhB molecules is highest at the 2L edge. Whereas the oxygen bonding (O<sup>2-</sup> of –COOH group) of RhB is highest at the 2L middle and 1L middle due to vacancies and nanopores. At Se vacancies, there is a bonding between one side

non-bonded Pd with O<sup>2-</sup> (–COOH group) of RhB form Pd–O bond. As Pd is a noble metal, the Pd–O bond produces a robust electronic coupling between the RhB molecule and the metal<sup>54</sup>. Se vacancies act as electron trapping sites for oxygen because oxygen has the same outermost electrons as Se. At the edge, there exists a smaller number of Pd termination, which gives rise to comparatively less Pd–O bond formation. As nanopore sizes are ~10–90 nm, the chemical adsorption is more at the active sites than the middle of the nanopore void. More physisorption is expected at the center of the nanopore. The size of the RhB molecule is ~1 nm, so 1L vacancy sites act as trapping sites for RhB, which makes vacancies quite interesting for SERS activity.

Further, we have performed SERS measurements of different concentrations of RhB molecule to calculate the detection efficiency of PdSe<sub>2</sub> dendrites. Figure 6c shows the SERS spectra of RhB with

different concentrations. The enhancement factor ( $EF$ ) in SERS sensing is calculated using the following equation,  $EF = \frac{I_{SERS}}{I_{RS}} \times \frac{C_{RS}}{C_{SERS}}$  where  $I_{SERS}$  and  $I_{RS}$  are the SERS and Raman signal (Supplementary Fig. 12) intensities, respectively, and  $C_{SERS}$ ,  $C_{RS}$  are the corresponding concentrations for which the intensities are considered. The calculated enhancement factor vs. RhB concentration log plot reflects a linear increment of  $EF$  as a function of concentration. It is evident that the pristine 2L PdSe<sub>2</sub> can serve as a SERS substrate with very low concentration ( $10^{-8}$  M) RhB detection with an enhancement factor of  $10^5$ . Such a high enhancement factor arises due to charge transfer between RhB molecules and PdSe<sub>2</sub> dendrites. To ascertain the same, the band positions of PdSe<sub>2</sub> were obtained using the cyclic voltammetry (CV) measurement (Supplementary Note 1 and Supplementary Fig. 13). PdSe<sub>2</sub> CBM and VBM are at  $-4.20$  eV and  $-5.52$  eV, respectively. It has been reported that the work function for ideal monolayer PdSe<sub>2</sub> is  $5.20$  eV<sup>55</sup>. However, from KPFM measurement, the measured work function of 1L and 2L PdSe<sub>2</sub> dendrites are  $4.83$  eV and  $4.87$  eV, respectively (Supplementary Note 2 and Supplementary Fig. 14). The lower work function is due to the presence of defect energy states in PdSe<sub>2</sub>. There exists a high density of electronic states at  $E_F$  because most edges of dendrites terminate with electron-rich Se. As the density of vacancies increases, additional defect states appear near the Fermi level. Thus, defect states are generated close to Fermi energy ( $E_F$ ). As a result, an additional charge transfer route between the RhB molecule and PdSe<sub>2</sub> is introduced.

A schematic illustration in Fig. 6c shows the corresponding energy levels and subsequent charge transfer mechanism. According to the literature, LUMO and HOMO energy value with respect to the vacuum of RhB is  $-3.08$  eV and  $-5.45$  eV, respectively<sup>56</sup>. When RhB is exposed to a laser excitation of  $532$  nm, the excitation energy is  $2.33$  eV which is less than or close to the energy difference between HOMO and LUMO ( $2.37$  eV) of RhB. This laser excitation energy is unable to amplify the Raman signal. When RhB/PdSe<sub>2</sub> hybrid system is exposed to  $532$  nm laser excitation, the charge transfer process may follow three possible paths. Absorption of a photon by RhB excites an electron from the highest occupied molecular orbital (HOMO) to the lowest unoccupied molecular orbital (LUMO) through Path 1 (Fig. 6c). Part of these charges may go to the conduction band (CB) of 2D PdSe<sub>2</sub> as depicted by the dashed curve in Fig. 6c and partly come back to the HOMO to recombine radiatively. Experimental evidence for the electron transfer from the RhB to PdSe<sub>2</sub> comes from the photoluminescence quenching of RhB, discussed later. Next, part of these electrons in CB of PdSe<sub>2</sub> may transfer to the HOMO of RhB through Path 2 and partly through Path 3, i.e., through the defect levels of PdSe<sub>2</sub>. The electronic transitions through Path 2 and Path 3 may cause lower energy recombination/emission, which is indeed reflected in the PL emission spectra discussed below for the hybrid system. Note that with the incident laser excitation, the electrons in PdSe<sub>2</sub> is also excited from the VB to the CB as well as to defect states and these electrons also partly follow Path 2 and Path 3 for relaxation. Thus, the transitions through Path 2 and Path 3 results in high density of electrons in the HOMO and LUMO of RhB, which gives rise to the highly intense Raman signal, i.e., SERS effect from RhB. A large amount of vacancy defects result in highly intense Raman modes<sup>26</sup>. Evidence of charge transfer and doping is further confirmed from the Raman spectrum. Figure 6d shows the stacked Raman spectra for pristine 2L PdSe<sub>2</sub> and RhB/2L PdSe<sub>2</sub> on mica substrate. Careful observation of Fig. 6d reveals that  $B_{1g}^1$  intensity increases in RhB/2L PdSe<sub>2</sub> system. The intensity ratio of  $A_g^1/B_{1g}^1$  is  $2.36$  in 2L PdSe<sub>2</sub>, which decreases to  $1.27$  in the RhB/2L PdSe<sub>2</sub> system. As the RhB injection mainly happens in Se vacancy sites, among all other modes  $B_{1g}^1$  mode becomes more intense due to the strongest coupling between RhB molecule with Se atoms. Peak shift in the Raman spectrum is a non-destructive way to understand the

doping, and charge transfer<sup>57,58</sup>. The spectral shift in Raman peak  $A_g^1$  ( $1.3$  cm<sup>-1</sup>) and  $A_g^3$  ( $1.6$  cm<sup>-1</sup>) in the RhB/2L PdSe<sub>2</sub> system is definite evidence of effective charge transfer in the hybrid system. Here charge transfer between RhB molecule and PdSe<sub>2</sub> was assumed to be the dominant factor which is accompanied by a large spectral shift in 2L PdSe<sub>2</sub>. For further confirmation, we have performed photoluminescence spectroscopy of the bare RhB and the RhB/2L PdSe<sub>2</sub> system (Fig. 6e). We notice a considerable redshift along with a significant quenching (68.7%) of photoluminescence spectrum in the hybrid system. The significant quenching may be attributed to the charge transfer from the RhB LUMO to CB and defect levels of 2D PdSe<sub>2</sub>. The redshift is a result of the lower energy transitions through Path 2 and Path 3, shown in Fig. 6c. Recently, Zhao et al. reported that for monolayer PdSe<sub>2</sub> with Se defect, there is a reduction in the bandgap and the band of midgap state goes through the Fermi level, and the PdSe<sub>2</sub> shows metal characteristics<sup>9</sup>. Series of Se<sub>TLU</sub> line vacancies in Fig. 2i in PdSe<sub>2</sub> act as metallic edge in the presence of excess Pd, similar to the report on extended defects in graphene acting as a metallic wire<sup>58</sup>.

To substantiate our conjecture, we performed DFT calculation of the band structure and density of states of the bilayer PdSe<sub>2</sub> system without and with line defects (Se vacancies). The details of the calculations are provided in the computational methods section. We have calculated the electronic properties of bilayer PdSe<sub>2</sub> without defect (2L PdSe<sub>2</sub>) and with line defects (defective 2L PdSe<sub>2</sub>) using PBE-GGA (Supplementary Figs. 15 and 16) and HSE06 (Fig. 7) functionals. Supplementary Fig. 15a and Fig. 7a represent the unit cell of 2L PdSe<sub>2</sub> and the side view of the defective 2L PdSe<sub>2</sub>, respectively. The calculated band structures along high symmetry k-points<sup>59</sup> illustrate an indirect bandgap of  $0.86$  eV in 2L PdSe<sub>2</sub> (Supplementary Fig. 15b), and the corresponding DOS is displayed in Supplementary Fig. 15c. Introduction of Se defects (edge) leads to drastic change in the band structure, where some bands are seen touching the Fermi level (Supplementary Fig. 16a), indicating the metallic characteristics of the defective 2L PdSe<sub>2</sub> system. The corresponding electronic density of states (DOS) is displayed in Supplementary Fig. 16b, which shows no bandgap and it confirms the metallic behavior of the system. Further, using  $3 \times 3$  supercell for PBE-GGA, we verified the electronic properties of the materials, and the DOS plot shown in Supplementary Fig. 16c also confirms the metallic properties of defective 2L PdSe<sub>2</sub>. Since the HSE06 functional provides a more accurate description of the band structure, we have calculated the band structure and the corresponding DOS of defective 2L PdSe<sub>2</sub> using HSE06 functional and the results are shown in Fig. 7b, c. It is evident from Fig. 7b that two different bands cross the Fermi energy ( $E_F$ ) along X-M and  $\Gamma$ -M direction and it indicates the metallic nature of defective 2L PdSe<sub>2</sub>. Interestingly, the density of states (DOS) plot reveals the electron occupation in the Fermi-level in the case of defective 2L PdSe<sub>2</sub>, which demonstrates the metallic feature of the material. When the RhB molecule is attached to such metallic edges, the quenching is maximum due to which we observed SERS associated PL signal with lower separation between molecule—Pd<sup>60</sup>. Quenching of photoluminescence suggests that there is a strong interaction between RhB molecule and defective PdSe<sub>2</sub>, which contributes to the efficient charge transfer in the RhB/2L PdSe<sub>2</sub> system. A redshift in the photoluminescence peak corresponds to lower energy emission. Due to defects and nanopores, charge transfer may take place to the lower energy, and subsequent recombination (through Path 2 and Path 3) may give rise to lower energy emission band. In Fig. 6d,  $B_{1g}^1$  mode is defect-related peak, which gets intense in 2L PdSe<sub>2</sub>/RhB. Thus, 2L edge sites are very crucial for the observed effect. Moreover, photoluminescence gives the intrinsic response of RhB/ 2L PdSe<sub>2</sub> system. Lin et al. reported the difference in photoluminescence fingerprint of Au nanorods and MGTIC molecule adsorbed Au nanorods<sup>61</sup>. Taking TEM analysis into account, some rows of Se<sub>TLU</sub> vacancies (Fig. 2i, j) along with excess

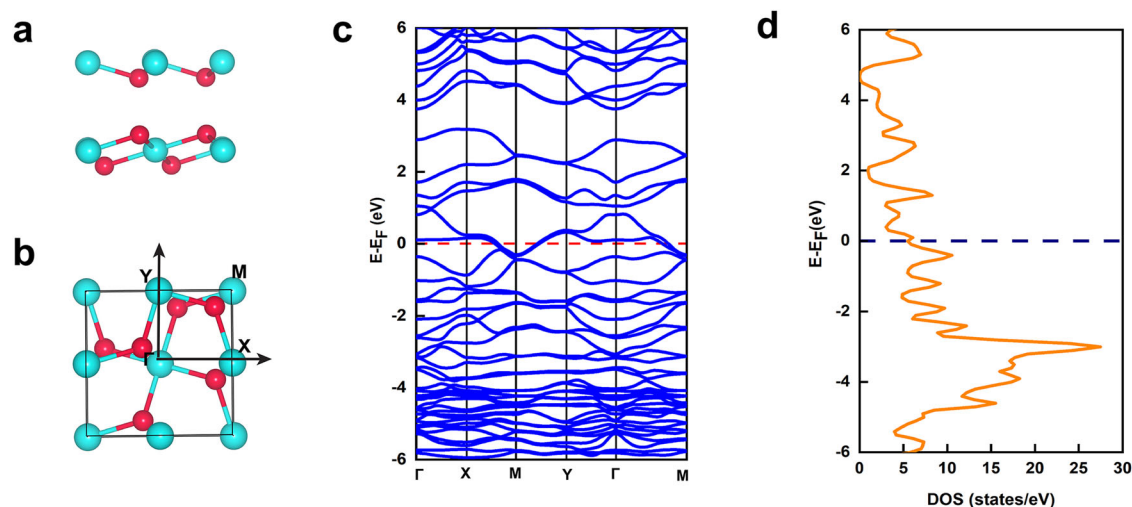


**Fig. 7** DFT calculation of defective PdSe<sub>2</sub>. **a** Unit cell (side view) of bilayer PdSe<sub>2</sub> with Se vacancy on the top layer (Se<sub>TLU</sub>). **b** Unit cell (top view) of defective 2L PdSe<sub>2</sub> showing the high symmetry K-points in the Brillouin zone. **c** Electronic band structure, and **d** DOS plot of defective 2L PdSe<sub>2</sub> using HSE06 functional showing metallic behavior. The Fermi level has been set to zero and indicated by the dashed line.

Pd behave like a metallic edge and acts as a defect-induced hotspot for SERS in detecting foreign molecules. Thus, the vacant sites in PdSe<sub>2</sub> basically act as a hotspot for SERS enhancement with RhB molecule. It is worth highlighting that we observed the PL emission peak along with the SERS signal of RhB/2L PdSe<sub>2</sub> system. Such photoluminescence-associated SERS signal retrieve a fingerprint of defects, and defective dendritic PdSe<sub>2</sub> acts as a defect-induced hotspot. Defect level close to the fermi-level produces a local doping site for RhB molecule in a narrow stripe along the line defect (created by Se<sub>TLU</sub> vacancies), which further contributes towards quasi-one dimensional metal-like behavior in 2d PdSe<sub>2</sub><sup>62</sup>. Orange fluorescence was observed over the 2D PdSe<sub>2</sub> dendrites denoting adsorption of Rhb molecule. Confocal microscopy imaging (inset of Fig. 6e) shows an altering contrast in fluorescence, which is due the plasmon-like behavior of vacancy-rich edges, line defects, and nanopores in dendritic PdSe<sub>2</sub>. To check the stability, we carried out SERS measurements after several months on 10<sup>-5</sup> M Rhodamine B deposited PdSe<sub>2</sub> sample, which was kept in the laboratory atmosphere (Supplementary Fig. 17). From the distinct Raman peak, it is clear that the samples are quite stable up to a few months. Any change in signal intensity is due to the partial evaporation of the dye molecules from the sample surface. To prove the versatility of the as-grown defect-rich 2L PdSe<sub>2</sub> dendrites as a very powerful SERS substrate, we have also carried out the SERS measurement with other molecules, such as methylene blue and methylene orange (10<sup>-4</sup> M, Supplementary Fig. 18). The result signifies its versatility for SERS detection with a variety of probe molecules. The strong Raman signals indicate a strong interaction between 2L dendritic PdSe<sub>2</sub> with probe molecules. Thus, it has the potential to be used as a commercial SERS substrate in the near future.

In summary, we demonstrated a simple low-temperature CVD synthesis technique to grow 2D PdSe<sub>2</sub> with attractive dendritic edges. Precise layer number and structure have been identified by AFM and Raman analyses. XPS analysis reveals about 9.3% outer layer Se vacancies, 4.7% inner Se vacancies, and 4.7% Pd vacancies in dendritic 2D PdSe<sub>2</sub>. Our finding, for the first time, shows a NIR photoluminescence from dendritic PdSe<sub>2</sub> and the influence of intrinsic defects on its bandgap. The comprehensive study on vacancies, nanopores, and edge geometry of PdSe<sub>2</sub> dendrites provides new insights into how intrinsic defects influence the properties. We speculate that Se vacancy sites in dendritic PdSe<sub>2</sub> behave as a metallic edge and it acts as a non-plasmonic hotspot for SERS detection of RhB molecule. Here, we have explained a defect

state-mediated charge transfer mechanism accompanied by a large spectral shift. To the best of our knowledge, this is the first report on high SERS activity on 2D PdSe<sub>2</sub> dendrites with extended defects. To validate our conjecture on the metallic behavior of the defective PdSe<sub>2</sub>, DFT calculations were performed for the electronic density of states in bilayer PdSe<sub>2</sub> with Se defects (edge) using PBE-GGA and HSE06 functionals and it clearly revealed metal-like behavior of the dendritic PdSe<sub>2</sub>. In the field of nanopore sensing applications, there exist two major limitations fundamental to conventional methods of fabricating nanopores: (i) high dependence on high-end instruments like STM, TEM to drill nanopores, (ii) only a single nanopore can be processed at a time. Therefore, there is a constant demand for a stable pore fabrication technique for the mass production of nanopores. Recently, Rani et al. reported a SERS enhancement up to ~10<sup>4</sup> at the sculpted plasmonic hotspots in monolayer MoS<sub>2</sub><sup>63</sup>. It has constantly been debated whether plasmon-free SERS substrate can compete with plasmonic SERS substrate. Interestingly, without any post-treatment, our plasmon-free dendritic PdSe<sub>2</sub> detects Rhodamine B (RhB) with a significant SERS enhancement (>10<sup>5</sup>); with post-growth treatment, it might exceed the plasmonic SERS substrate limit. Our findings offer insights into the field of SERS sensing, nanopore sensing, gas sensing, biosensing, and device fabrication applications, where we believe PdSe<sub>2</sub> will be a rising star in the near future. The observations, analysis, and related findings presented here show the trivial nature of dendritic PdSe<sub>2</sub>, which can be expected to replace the existing plasmon-free SERS substrates in high demand in the coming generation and blossom into the affluent area of commercial products.

## METHODS

### Low-temperature CVD growth of PdSe<sub>2</sub> dendrites

All precursors were purchased from Sigma Aldrich and used for experiments without further purification. We adopted a novel synthesis technique with a slight addition of NaCl to obtain dendritic PdSe<sub>2</sub><sup>45</sup>. Briefly, we followed a two-step process, (i) PdCl<sub>2</sub> solution preparation (with adding a small amount of NaCl) and (ii) relatively low-temperature chemical vapor deposition. Firstly, we dissolve PdCl<sub>2</sub> powder (99.999%, 27 mg) in Milli Q water. When the powder was dissolved entirely, NaCl was added and stirred to dissolve completely. Then it is kept for a few hours for further use in CVD. Secondly, the solution is drop-casted on the freshly cleaved mica substrate and heated on a hot plate in atmospheric conditions to use as a CVD substrate. To conduct the CVD process, a single-zone

tube furnace was used. Then, the as-prepared substrate was inserted into the quartz tube and placed at the lower temperature zone. At the center of the tube, Se precursors were kept. A rotary pump was used to evacuate the quartz tube, and Argon was purged with 300 sccm to pump out other residues from the tube. Then the furnace temperature was elevated to 450 °C to vaporize the Se precursor, and a flow rate of 110 sccm was introduced to carry the precursor to the substrate for nucleation and growth of PdSe<sub>2</sub> film.

### SERS measurement

Water solutions of RhB were prepared with different concentrations by diluting sequentially. Further, it was drop-casted over the CVD-grown PdSe<sub>2</sub> dendrites and kept for a few minutes to soak up the RhB molecule completely. An excitation source of 532 nm equipped with the Raman instruments (LabRam HR800, Jobin Yvon) was used to obtain the SERS spectra on PdSe<sub>2</sub>.

### Sample preparation for TEM characterization

The as-prepared samples were transferred to the TEM grid following our previous report<sup>45</sup>. In short, PMMA based transfer process has been conducted. First, PMMA was spin-coated on the PdSe<sub>2</sub> dendrites, followed by drying. After that, it was immersed into a KOH solution till the lift-off of PMMA/PdSe<sub>2</sub> from mica substrate. Further, it was dipped into deionized water. Then the floated PMMA/PdSe<sub>2</sub> was scooped with the carbon-coated Cu-grid (300 mesh, pacific grid, USA). After that, it is rinsed with acetone to remove PMMA, followed by IPA cleaning.

### Characterization technique

The structural morphology is obtained using field emission electron microscopy (FESEM, Sigma, Zeiss). The as-grown sample thickness was estimated via atomic force microscopy (AFM) (Cypher, Oxford Instruments) in non-contact mode scanning. KPFM measurement was performed on conducting surface (ITO-coated glass) with Ti/Ir-coated silicon tip in the AFM instrument above. The high-magnification surface morphology of dendritic PdSe<sub>2</sub> has been carried out by a transmission electron microscope (TEM) (JEOL-JEM 2010 operated at 200 kV). The samples for TEM analysis have been prepared on a carbon-coated Cu-grid of 300 mesh size (Pacific Grid, USA). The crystallinity in the as-grown PdSe<sub>2</sub> flakes has been studied by high-resolution micro-Raman spectroscopy (LabRam HR800, Jobin Yvon) with an excitation wavelength ( $\lambda_{ex}$ ) of 532 nm (Ar ion laser). The excitation laser light was focused with a 100X objective lens to a spot size of 1  $\mu$ m, with a laser power of 1.5 mW, which discards the possibility of laser heating-induced damage. A charge-coupled device equipped with the same system collected the signal in a backscattering geometry sent through a multimode fiber grating of 1800 grooves mm<sup>-1</sup>. Micro-PL in PdSe<sub>2</sub>/RhB and RhB have been conducted in the Raman instrument with 532 nm laser excitation. X-ray photoelectron spectroscopy (XPS) measurement was executed using a PHI X-tool automated photoelectron spectrometer (ULVAC-PHI, Japan) with an Al K $\alpha$  X-ray beam (1486.6 eV) at 20 kV, 84 W for the analysis of the chemical compositions. NIR PL has been taken with laser excitation 641 nm with a power of 50 mW. Confocal microscopy imaging was performed with 488 nm laser excitation (Zeiss LSM 880).

### Computational methods

The calculation of the electronic properties of the bilayer PdSe<sub>2</sub> without and with line defects were performed within the framework of density functional theory (DFT), including van der Waals Correction (vdW) with a plane-wave basis set using Quantum ESPRESSO software<sup>64–66</sup>. The core electrons were described using the projector-augmented-wave (PAW) pseudopotentials<sup>67</sup>, and the exchange-correlation potential was estimated using the generalized gradient approximation (GGA) with Perdew–Burke–Ernzerhof (PBE)<sup>68</sup>

functional. To model, the Se defect in 2L PdSe<sub>2</sub> structures were built by a periodic slab geometry with a vacuum of 20 Å along the Z-direction. Subsequently, the upper Se-atom present in the upper layer of the slab was removed from the unit cell and obtained the desired structure (defective 2L PdSe<sub>2</sub>). The optimized lattice constants of the unit cell of defective 2L PdSe<sub>2</sub> were  $a = 5.72$  Å and  $b = 5.80$  Å which are slightly lower than those of pristine 2L PdSe<sub>2</sub> ( $a = 5.75$ , and  $b = 5.87$ )<sup>8</sup>. Using a convergence test, a  $12 \times 12 \times 1$  k-point sampling was employed with cut-off energy of 680 eV. Additionally, the band structure as well as the DOS of the defective 2L PdSe<sub>2</sub> were calculated using the HSE06 exchange hybrid functional as it provides a more accurate description of the band structure<sup>69</sup>. Then  $3 \times 3 \times 1$  supercells of pristine 2L PdSe<sub>2</sub> and defective 2L PdSe<sub>2</sub> were constructed with k-point sampling  $8 \times 8 \times 1$ . To achieve self-consistency, a force of 10<sup>-2</sup> eV/Å was employed.

### DATA AVAILABILITY

The data that support the findings of this study are available in the Supplementary Information file.

Received: 10 May 2022; Accepted: 13 January 2023;

Published online: 06 February 2023

### REFERENCES

- Pi, L. et al. Recent progress on 2D noble-transition-metal dichalcogenides. *Adv. Funct. Mater.* **29**, 1904932 (2019).
- Kuklin, A. V. & Ågren, H. Quasiparticle electronic structure and optical spectra of single-layer and bilayer PdSe<sub>2</sub>: proximity and defect-induced band gap renormalization. *Phys. Rev. B* **99**, 245114 (2019).
- Zhang, X. et al. Centimeter-scale few-layer PdSe<sub>2</sub>: fabrication and physical properties. *ACS Appl. Mater. Interfaces* **13**, 43063–43074 (2021).
- Aftab, S. et al. Switching photodiodes based on (2D/3D) PdSe<sub>2</sub>/Si heterojunctions with a broadband spectral response. *J. Mater. Chem. C* **9**, 3998–4007 (2021).
- Aftab, S. et al. Platinum disulfide (PtS<sub>2</sub>) and silicon pyramids: efficient 2D/3D heterojunction tunneling and breakdown diodes. *ACS Appl. Electron. Mater.* **4**, 917–924 (2022).
- Aftab, S. et al. Single nanoflake-based PtSe<sub>2</sub> p–n junction (in-plane) formed by optical excitation of point defects in BN for ultrafast switching photodiodes. *J. Mater. Chem. C* **9**, 199–207 (2021).
- Pi, L. et al. Highly in-plane anisotropic 2D PdSe<sub>2</sub> for polarized photodetection with orientation selectivity. *Adv. Funct. Mater.* **31**, 2006774 (2021).
- Oyedele, A. D. et al. PdSe<sub>2</sub>: pentagonal two-dimensional layers with high air stability for electronics. *J. Am. Chem. Soc.* **139**, 14090–14097 (2017).
- Zhao, Y. et al. Low-symmetry PdSe<sub>2</sub> for high performance thermoelectric applications. *Adv. Funct. Mater.* **30**, 2004896 (2020).
- Lu, L.-S. et al. Layer-dependent and in-plane anisotropic properties of low-temperature synthesized few-layer PdSe<sub>2</sub> single crystals. *ACS Nano* **14**, 4963–4972 (2020).
- Illarionov, Y. Y. et al. Long-term stability and reliability of black phosphorus field-effect transistors. *ACS Nano* **10**, 9543–9549 (2016).
- Wood, J. D. et al. Effective passivation of exfoliated black phosphorus transistors against ambient degradation. *Nano Lett.* **14**, 6964–6970 (2014).
- Mermin, N. D. Crystalline order in two dimensions. *Phys. Rev.* **176**, 250–254 (1968).
- Novoselov, K. S. et al. Electric field effect in atomically thin carbon films. *Science* **306**, 666–669 (2004).
- Terrones, H., Lv, R., Terrones, M. & Dresselhaus, M. S. The role of defects and doping in 2D graphene sheets and 1D nanoribbons. *Rep. Prog. Phys.* **75**, 062501 (2012).
- Zhou, W. et al. Intrinsic structural defects in monolayer molybdenum disulfide. *Nano Lett.* **13**, 2615–2622 (2013).
- Xu, X., Robertson, J. & Li, H. Semiconducting few-layer PdSe<sub>2</sub> and Pd<sub>2</sub>Se<sub>3</sub>: native point defects and contacts with native metallic Pd<sub>17</sub>Se<sub>15</sub>. *Phys. Chem. Chem. Phys.* **22**, 7365–7373 (2020).
- Oyedele, A. D. et al. Defect-mediated phase transformation in anisotropic two-dimensional PdSe<sub>2</sub> crystals for seamless electrical contacts. *J. Am. Chem. Soc.* **141**, 8928–8936 (2019).
- Zhao, X. W. et al. Tuning electronic and optical properties of monolayer PdSe<sub>2</sub> by introducing defects: first-principles calculations. *Sci. Rep.* **10**, 4028 (2020).
- Shautsova, V. et al. Direct laser patterning and phase transformation of 2D PdSe<sub>2</sub> films for on-demand device fabrication. *ACS Nano* **13**, 14162–14171 (2019).

21. Nguyen, G. D. et al. 3D imaging and manipulation of subsurface selenium vacancies in PdSe<sub>2</sub>. *Phys. Rev. Lett.* **121**, 086101 (2018).
22. Jakhar, M., Singh, J., Kumar, A. & Pandey, R. First-principles study of the hexagonal T-phase PdSe<sub>2</sub> monolayer and its application in solar cells. *J. Phys. Chem. C* **124**, 26565–26571 (2020).
23. Fu, M. et al. Defects in highly anisotropic transition-metal dichalcogenide PdSe<sub>2</sub>. *J. Phys. Chem. Lett.* **11**, 740–746 (2020).
24. Liang, Q., Zhang, Q., Zhao, X., Liu, M. & Wee, A. T. S. Defect engineering of two-dimensional transition-metal dichalcogenides: applications, challenges, and opportunities. *ACS Nano* **15**, 2165–2181 (2021).
25. Zheng, Z. et al. Semiconductor SERS enhancement enabled by oxygen incorporation. *Nat. Commun.* **8**, 1993 (2017).
26. Lin, J. et al. Ultrasensitive SERS detection by defect engineering on single Cu<sub>2</sub>O superstructure particle. *Adv. Mater.* **29**, 1604797 (2017).
27. Cong, S. et al. Noble metal-comparable SERS enhancement from semiconducting metal oxides by making oxygen vacancies. *Nat. Commun.* **6**, 7800 (2015).
28. Danda, G. & Drndić, M. Two-dimensional nanopores and nanoporous membranes for ion and molecule transport. *Curr. Opin. Biotechnol.* **55**, 124–133 (2019).
29. Liu, K. et al. Geometrical effect in 2D nanopores. *Nano Lett.* **17**, 4223–4230 (2017).
30. Garoli, D., Yamazaki, H., Maccaferri, N. & Wanunu, M. Plasmonic nanopores for single-molecule detection and manipulation: toward sequencing applications. *Nano Lett.* **19**, 7553–7562 (2019).
31. Qiu, H., Zhou, W. & Guo, W. Nanopores in graphene and other 2D materials: a decade's journey toward sequencing. *ACS Nano* **15**, 18848–18864 (2021).
32. Lee, K. et al. Recent progress in solid-state nanopores. *Adv. Mater.* **30**, 1704680 (2018).
33. Su, S., Wang, X. & Xue, J. Nanopores in two-dimensional materials: accurate fabrication. *Mater. Horiz.* **8**, 1390–1408 (2021).
34. Wanunu, M. & Meller, A. Chemically modified solid-state nanopores. *Nano Lett.* **7**, 1580–1585 (2007).
35. Lan, L., Hou, X., Gao, Y., Fan, X. & Qiu, T. Inkjet-printed paper-based semiconducting substrates for surface-enhanced Raman spectroscopy. *Nanotechnology* **31**, 055502 (2019).
36. Qiu, Y. et al. Photodegradable CuS SERS probes for intraoperative residual tumor detection, ablation, and self-clearance. *ACS Appl. Mater. Interfaces* **11**, 23436–23444 (2019).
37. Alvarez-Puebla, R. A. & Liz-Marzán, L. M. SERS detection of small inorganic molecules and ions. *Angew. Chem. Int. Ed.* **51**, 11214–11223 (2012).
38. Han, X. X., Ji, W., Zhao, B. & Ozaki, Y. Semiconductor-enhanced Raman scattering: active nanomaterials and applications. *Nanoscale* **9**, 4847–4861 (2017).
39. Shankla, M. & Aksimentiev, A. Step-defect guided delivery of DNA to a graphene nanopore. *Nat. Nanotechnol.* **14**, 858–865 (2019).
40. Danda, G. et al. Monolayer WS<sub>2</sub> nanopores for DNA translocation with light-adjustable sizes. *ACS Nano* **11**, 1937–1945 (2017).
41. Zhang, L. & Wang, X. DNA sequencing by hexagonal boron nitride nanopore: a computational study. *Nanomaterials* **6**, 111 (2016).
42. Masih Das, P. et al. Controlled sculpture of black phosphorus nanoribbons. *ACS Nano* **10**, 5687–5695 (2016).
43. Govind Rajan, A. et al. Addressing the isomer cataloguing problem for nanopores in two-dimensional materials. *Nat. Mater.* **18**, 129–135 (2019).
44. Vicarelli, L., Heerema, S. J., Dekker, C. & Zandbergen, H. W. Controlling defects in graphene for optimizing the electrical properties of graphene nanodevices. *ACS Nano* **9**, 3428–3435 (2015).
45. Jena, T., Hossain, M. T. & Giri, P. K. Temperature-dependent Raman study and determination of anisotropy ratio and in-plane thermal conductivity of low-temperature CVD-grown PdSe<sub>2</sub> using unpolarized laser excitation. *J. Mater. Chem. C* **9**, 16693–16708 (2021).
46. Yu, J. et al. Giant nonlinear optical activity in two-dimensional palladium diselenide. *Nat. Commun.* **12**, 1083 (2021).
47. Liang, Q. et al. Performance Improvement by ozone treatment of 2D PdSe<sub>2</sub>. *ACS Nano* **14**, 5668–5677 (2020).
48. Hoffman, A. N. et al. Exploring the air stability of PdSe<sub>2</sub> via electrical transport measurements and defect calculations. *npj 2D Mater. Appl* **3**, 50 (2019).
49. Banhart, F., Kotakoski, J. & Krasheninnikov, A. V. Structural defects in graphene. *ACS Nano* **5**, 26–41 (2011).
50. Jeong, M.-H. et al. Multilayer WSe<sub>2</sub>/MoS<sub>2</sub> heterojunction phototransistors through periodically arrayed nanopore structures for bandgap engineering. *Adv. Mater.* **34**, 2108412 (2022).
51. Merchant, C. A. et al. DNA translocation through graphene nanopores. *Nano Lett.* **10**, 2915–2921 (2010).
52. Koskinen, P., Malola, S. & Häkkinen, H. Self-passivating edge reconstructions of graphene. *Phys. Rev. Lett.* **101**, 115502 (2008).
53. Huang, Q. et al. Flower-like molybdenum disulfide for polarity-triggered accumulation/release of small molecules. *ACS Appl. Mater. Interfaces* **9**, 36431–36437 (2017).
54. Karthick Kannan, P., Shankar, P., Blackman, C. & Chung, C.-H. Recent advances in 2D inorganic nanomaterials for SERS sensing. *Adv. Mater.* **31**, 1803432 (2019).
55. Liu, X., Zhou, H., Yang, B., Qu, Y. & Zhao, M. Strain-modulated electronic structure and infrared light adsorption in palladium diselenide monolayer. *Sci. Rep.* **7**, 39995 (2017).
56. Qiu, H. et al. Wrinkled 2H-phase MoS<sub>2</sub> sheet decorated with graphene-microflowers for ultrasensitive molecular sensing by plasmon-free SERS enhancement. *Sens. Actuators B Chem.* **320**, 128445 (2020).
57. Dhakal, K. P. et al. Confocal absorption spectral imaging of MoS<sub>2</sub>: optical transitions depending on the atomic thickness of intrinsic and chemically doped MoS<sub>2</sub>. *Nanoscale* **6**, 13028–13035 (2014).
58. Hossain, M. T., Das, M., Ghosh, J., Ghosh, S. & Giri, P. K. Understanding the interfacial charge transfer in the CVD grown Bi<sub>2</sub>O<sub>2</sub>Se/CsPbBr<sub>3</sub> nanocrystal heterostructure and its exploitation in superior photodetection: experiment vs. theory. *Nanoscale* **13**, 14945–14959 (2021).
59. Zhao, X. et al. Electronic and optical properties of PdSe<sub>2</sub> from monolayer to trilayer. *Superlattices Microstruct.* **142**, 106514 (2020).
60. Johansson, P., Xu, H. & Käll, M. Surface-enhanced Raman scattering and fluorescence near metal nanoparticles. *Phys. Rev. B* **72**, 035427 (2005).
61. Lin, K.-Q. et al. Plasmonic photoluminescence for recovering native chemical information from surface-enhanced Raman scattering. *Nat. Commun.* **8**, 14891 (2017).
62. Lahiri, J., Lin, Y., Bozkurt, P., Oleynik, I. I. & Batzill, M. An extended defect in graphene as a metallic wire. *Nat. Nanotechnol.* **5**, 326–329 (2010).
63. Rani, R. et al. Sculpting artificial edges in monolayer MoS<sub>2</sub> for controlled formation of surface-enhanced Raman hotspots. *ACS Nano* **14**, 6258–6268 (2020).
64. Kresse, G. & Furthmüller, J. Efficient iterative schemes for ab initio total-energy calculations using a plane-wave basis set. *Phys. Rev. B* **54**, 11169–11186 (1996).
65. Parr, R. G. Density functional theory. *Annu. Rev. Phys. Chem.* **34**, 631–656 (1983).
66. Giannozzi, P. et al. QUANTUM ESPRESSO: a modular and open-source software project for quantum simulations of materials. *J. Phys. Condens. Matter* **21**, 395502 (2009).
67. Blöchl, P. E. Projector augmented-wave method. *Phys. Rev. B* **50**, 17953–17979 (1994).
68. Perdew, J. P., Burke, K. & Ernzerhof, M. Generalized gradient approximation made simple. *Phys. Rev. Lett.* **77**, 3865–3868 (1996).
69. Heyd, J., Scuseria, G. E. & Ernzerhof, M. Hybrid functionals based on a screened Coulomb potential. *J. Chem. Phys.* **118**, 8207–8215 (2003).

## ACKNOWLEDGEMENTS

The central instrumental facility, IIT Guwahati, is greatly acknowledged for TEM, AFM, and FESEM facilities. PKG acknowledges the financial support from MEITY (Grant No. 5(1)/2021-NANO) and SERB (Grant number CRG/2021/006397) for carrying out part of this work. HS and MF acknowledge the support from Kobe University Strategic International Collaborative Research Grant (Type B Fostering Joint Research). UN and MS thank the PARAM-ISHAN super-computing facilities and the Department of Chemistry, IIT Guwahati, for infrastructure facilities. UN acknowledges the support from the Department of Science and Technology (DST), India, for an INSPIRE Fellowship. (No. DST/INSPIRE Fellowship/2018/IF180745).

## AUTHOR CONTRIBUTIONS

T.J., M.T.H., and P.K.G. conceptualized the work. T.J. and M.T.H. performed the experiments. T.J., U.N., and M.S. performed the theoretical calculations. H.S. and M.F. carried out the XPS and NIR PL measurements. U.N. and M.S. interpreted the theoretical results. T.J., M.T.H., and P.K.G. interpreted the experimental/theoretical results and wrote the manuscript draft, and all the authors contributed to the final version of the manuscript.

## COMPETING INTERESTS

The authors declare no competing interests.

## ADDITIONAL INFORMATION

**Supplementary information** The online version contains supplementary material available at <https://doi.org/10.1038/s41699-023-00367-3>.

**Correspondence** and requests for materials should be addressed to P. K. Giri.

**Reprints and permission information** is available at <http://www.nature.com/reprints>

**Publisher's note** Springer Nature remains neutral with regard to jurisdictional claims in published maps and institutional affiliations.



**Open Access** This article is licensed under a Creative Commons Attribution 4.0 International License, which permits use, sharing, adaptation, distribution and reproduction in any medium or format, as long as you give appropriate credit to the original author(s) and the source, provide a link to the Creative Commons license, and indicate if changes were made. The images or other third party material in this article are included in the article's Creative Commons license, unless indicated otherwise in a credit line to the material. If material is not included in the article's Creative Commons license and your intended use is not permitted by statutory regulation or exceeds the permitted use, you will need to obtain permission directly from the copyright holder. To view a copy of this license, visit <http://creativecommons.org/licenses/by/4.0/>.

© The Author(s) 2023